



Initial Results from a Systematic Search for Changing-look Active Galactic Nuclei Selected via Mid-infrared Variability

Zhenfeng Sheng^{1,2}, Tinggui Wang^{1,2}, Ning Jiang^{1,2}, Jiani Ding³, Zheng Cai^{3,4}, Hengxiao Guo^{5,6}, Luming Sun^{1,2},
Liming Dou⁷, and Chenwei Yang⁸

¹ CAS Key Laboratory for Researches in Galaxies and Cosmology, University of Sciences and Technology of China, Hefei, Anhui 230026, People's Republic of China; shengzf@ustc.edu.cn, twang@ustc.edu.cn

² School of Astronomy and Space Science, University of Science and Technology of China, Hefei 230026, People's Republic of China

³ Department of Astronomy & Astrophysics, University of California Santa Cruz, 1156 High Street, Santa Cruz, CA, 95064, USA

⁴ UCO/Lick Observatory, University of California, 1156 High Street, Santa Cruz, CA, 95064, USA

⁵ Department of Astronomy, University of Illinois at Urbana-Champaign, Urbana, IL 61801, USA

⁶ National Center for Supercomputing Applications, University of Illinois at Urbana-Champaign, Urbana, IL 61801, USA

⁷ Center for Astrophysics, Guangzhou University, Guangzhou 510006, People's Republic of China

⁸ SOA Key Laboratory for Polar Science, Polar Research Institute of China, 451 Jinqiao Road, Shanghai, 200136, People's Republic of China

Received 2019 April 30; revised 2019 November 4; accepted 2019 November 22; published 2020 January 23

Abstract

Changing-look active galactic nuclei (CL AGNs) can yield considerable insight into accretion physics as well as the co-evolution of black holes and their host galaxies. A large sample of these CL AGNs is essential to achieve the latter goal. We propose an effective method to select CL candidates from spectroscopic quasar catalogs using the mid-infrared (MIR) variability information derived from ALLWISE/NEOWISE data releases. Our primary selection criteria include both a large amplitude flux variation and a transition of MIR color from an AGN to a normal galaxy. A pilot spectroscopic follow-up of seven candidates among about 300 candidates selected from Sloan Digital Sky Survey low-redshift ($z < 0.5$) AGN sample results in three new turn-off CL AGNs and three ambiguous objects for suffering low spectral quality. We expect to obtain hundreds of CL AGNs once full spectroscopic follow-up of the sample is carried out.

Unified Astronomy Thesaurus concepts: Active galaxies (17); Infrared galaxies (790); Galaxy nuclei (609)

1. Introduction

Changing-look active galactic nuclei (CL AGNs) are sources that can exhibit a transition from Type 1 to Type 1.8, 1.9, and 2 or vice versa, featuring disappearing or emerging broad emission lines (BELs) on timescales of months to years (LaMassa et al. 2015; MacLeod et al. 2016; Ruan et al. 2016; Runnoe et al. 2016; Gezari et al. 2017). These sources were once serendipitously discovered in nearby AGNs (e.g., Cohen et al. 1986; Storchi-Bergmann et al. 1993; Eracleous & Halpern 2001; Denney et al. 2014; Shappee et al. 2014). With the repeated spectroscopic observations, the number of CL AGNs has increased rapidly in recent years (MacLeod et al. 2016, 2019; Ruan et al. 2016; Yang et al. 2018; Oknyansky et al. 2019).

The origin of CL AGNs is still underdebated. There are three general explanations: variation in obscuration (e.g., Goodrich 1989; Tran et al. 1992), accretion rate change (e.g., LaMassa et al. 2015), or Tidal Disrupted Event (TDE; Merloni et al. 2015). However, due to the recent observation evidence, the rapid changes in black hole accretion rate is preferred. For example, both short transition timescale and dramatic optical/infrared variation of CL AGNs are inconsistent with the variable obscuration (LaMassa et al. 2015; MacLeod et al. 2016; Gezari et al. 2017; Sheng et al. 2017; Wang et al. 2018); low level polarization of CL AGNs suggests the disappearance of the BELs cannot be attributed to dust obscuration (Hutsemékers et al. 2017, 2019). Furthermore, the optical light curves of the most CL AGNs usually show no TDE-like power-law decay feature ($t^{-5/3}$, e.g., Rees 1988), and their spectra often resemble a typical AGN spectrum rather than TDE-like with strong He II emission line (e.g., Gezari et al. 2012).

Even though it is widely suggested that some instabilities in the accretion disk are responsible for the CL mechanism. The driving mechanism itself has pushed the standard viscous accretion disk model into a crisis (Lawrence 2018), for the accretion theory failed to predict the proper CL transition timescale. Several alternative models have been proposed to explain the CL phenomena, such as X-binary-like accretion (Ruan et al. 2019); magnetically elevated accretion (Dexter & Begelman 2019); and the narrow transition zone between the standard disk and inner advection dominated accretion flow (Śniegowska & Czerny 2019).

While studying the CL mechanism of AGNs is of particular importance for understanding the structure and physics of accretion disk, CL AGNs also provide an ideal case of investigating the connection between AGNs and their host galaxies such as studying the $M_{\text{BH}} - \sigma_*$ (Gezari et al. 2017) or the host of a bright AGN whose starlight is overwhelmed by a luminous central engine. Furthermore, the timescale and frequency of the transition could help to restrict the lifetimes of AGNs (Martini & Schneider 2003). So an extensive sample of these CL AGNs is essential to address the above questions.

So far, more than 50 CL AGNs have been reported. There are several notable works for finding CL AGNs. For example, mining the archival spectra in the Sloan Digital Sky Survey (SDSS) among quasars with repeated spectra, two and ten CL AGNs have been identified by Ruan et al. (2016) and MacLeod et al. (2016), respectively. Also, Yang et al. (2018) identified 21 new CL AGNs through a similar method. CL AGNs may be surprisingly common. Runco et al. (2016) study 102 local Seyfert galaxies and find that $\sim 38\%$ of sources show type change, and the $H\beta$ completely disappeared in three objects. Recently, Rumbaugh et al. (2018) found that extremely

variable ($\Delta g > 1$) AGNs account for 30% \sim 50% of quasars. Meanwhile, MacLeod et al. (2019) reported 16 new CL AGNs, yielding a confirmation rate of \sim 20%, based on photometric variation selection ($\Delta g > 1$ and $\Delta r > 0.5$ mag) followed by new spectroscopic observations.

Besides the photometric variation selection method as MacLeod et al. (2019) performed, mid-infrared (MIR) monitoring also provides a powerful tool for finding CL AGNs candidates, and for investigating their physical processes. In our previous work, we investigated 10 CL AGNs (Sheng et al. 2017) using the MIR multi-photometric monitoring data from *Wide-field Infrared Survey Explorer* (*WISE*; Wright et al. 2010) and the Near-Earth Object *WISE* Reactivation mission (*NEOWISE-R*; Mainzer et al. 2014). We found all the 10 CL AGNs have strong (>0.4 mag) variability in MIR bands and have a transition from Type 1 to Type 2, accompanied by changing from AGN-like MIR color ($W1 - W2 > 0.8$) to galaxy-like MIR color ($W1 - W2 < 0.5$; Stern et al. 2012; Yan et al. 2013), and vice versa. Meanwhile, the large variability amplitude supports the scheme of dramatic change in the accretion rate. Recently, with large monotonic variation in either $W1$ or $W2$ (Stern et al. 2018) reported a new CL AGN J105203.55+151929.5. In addition, Assef et al. (2018a, 2018b) presented two catalogs of AGNs selected from *WISE*'s AllWISE database and found two of the highest variability candidates (WISEA J142846.71+172353.1, J094806.56+031801.7) were CL AGNs.

Following our previous work, here we propose a method of selecting candidates of CL AGNs based on MIR variation and color change. With this method, we find a large sample of CL AGNs candidates. We followed seven candidates that are bright and proper for observation. Finally, six new CL AGNs are identified. The outline of this paper is as follows. In Section 2, we describe the selection method, and the data/spectra used in this study. In Section 3, we describe the spectral decomposition and present the results. We will make a simple discussion in Section 4. Then we come to a summary in Section 5. We adopt a flat Λ CDM cosmology with $H_0 = 70 \text{ km s}^{-1} \text{ Mpc}^{-1}$ and $\Omega_m = 0.3$.

2. Data

2.1. Sample Selection

Our selection criteria aimed at finding good candidates of CL AGNs which had already been spectroscopically identified as AGNs with archival SDSS. We start from the catalog of all SDSS spectra named as “*specObj-dr14*.”⁹ We cull the sources that were classified as “QSO” and the redshift is below 0.5 (because we would like to monitor both $H\beta$ and $H\alpha$). Using the Tool for OPERations on Catalogs And tables (TOPCAT; Taylor 2005), we get 63,860 “QSO” sources. We match the DR7, DR12, and Dr14 quasar catalogs (Schneider et al. 2010; Pâris et al. 2017, 2018), and find another 307 sources ($z \leq 0.5$) not included in the “*specObj-dr14*” quasar catalog. So we have a sample of 64,167 quasar sources. In addition, we also match the 14,584 broad-line AGNs ($z \leq 0.35$) selected from complete DR7 database (Liu et al. 2019) and find another 2864 sources. So totally we have 67,031 objects, which were once classified as broad-line AGNs.

We download the multi-epoch photometric data of *WISE* and *NEOWISE* from NASA/IPAC Infrared Science Archive for the whole sample, and extracted mid-IR $W1$ ($3.4 \mu\text{m}$) and

$W2$ ($4.6 \mu\text{m}$) light curves. After checking the MIR data, there were 39,858 objects that had both light curves in AllWISE and *NEOWISE* epoch. We constrain that the CL AGN candidates should have both significant MIR variation and color transition. So the sources are further screened according to the following criteria:

- (1) The MIR light curves should have linear correlation for consistent variation trends. So we calculated the Pearson correlation coefficient between $W1$ and $W2$ bands for each object, and removed 25,779 objects whose correlation coefficient $r < 0.8$.
- (2) The candidates should be bright to have good photometric accuracy, so we constrain that the mean value of $W1$ band in *NEOWISE* epoch is brighter than 15 mag. In the process, 961 objects are excluded.
- (3) The MIR color of turn-off AGNs likely change from AGN-like to galaxy-like (Stern et al. 2012; Yan et al. 2013; Sheng et al. 2017), along with the decrease of MIR luminosity. So we constrain that the mean value of color ($W1 - W2$) in AllWISE epoch is 0.1 larger than that in *NEOWISE* epoch at 3σ significance (the error is calculated by the propagation method). Meanwhile, we further constrain that the mean value of $W1$ and $W2$ bands in AllWISE epoch are brighter than those in *NEOWISE* epoch. In the process, 12,629 objects are removed.
- (4) The MIR color $W1 - W2 > 0.8$ is usually used to select AGNs (e.g., Stern et al. 2012; Assef et al. 2013). The sources whose minimum value of $W1 - W2$ is above this value should be abandoned, for they likely maintain strong Balmer emission lines. Here we further exclude 46 objects.
- (5) In our previous work we have found CL AGNs have strong (>0.4 mag) variability in MIR light curves and color changing along with the type transition. So we finally constrain that the MIR amplitude of the candidates is larger than 0.4 mag at more than 5σ significance in either $W1$ or $W2$ bands. In this process, 90 objects are removed.

Finally, we get 353 candidates. The distribution of MIR color variability, $W1$ and $W2$ variability of the sample, are presented in Figure 1.

We took optical spectra of seven candidates that are bright and proper for observation in June of 2018: J1252+5918, J1307+4506, J1317+1024, J1428+1723, J1549+1121, J1627+5419, J1713+2736 (full name see column 1 in Table 1).

2.2. Light Curves

The *WISE* mission surveyed the entire sky in four infrared wavelengths centered at 3.4, 4.6, 12, and 22 μm (denoted $W1$, $W2$, $W3$, and $W4$) from 2010 January to September, until its cryogen used to cool the $W3$ and $W4$ channels were depleted. After an extended four months of Post-Cryogenic Mission, it was then placed into hibernation. On 2013 October 3, it was reactivated as *NEOWISE-R*, surveying the sky at $W1$ and $W2$ (Mainzer et al. 2014). So there is a gap between *WISE* and *NEOWISE* epoch. With a polar orbit, *WISE/NEOWISE* scan the entire sky every 6 months and provide \sim 12 observations per half year for the most sources. Following our previous work (Jiang et al. 2012, 2016; Sheng et al. 2017), we removed bad data points with poor image quality (“qi_fact” < 1), a

⁹ https://www.sdss.org/dr14/spectro/spectro_access/

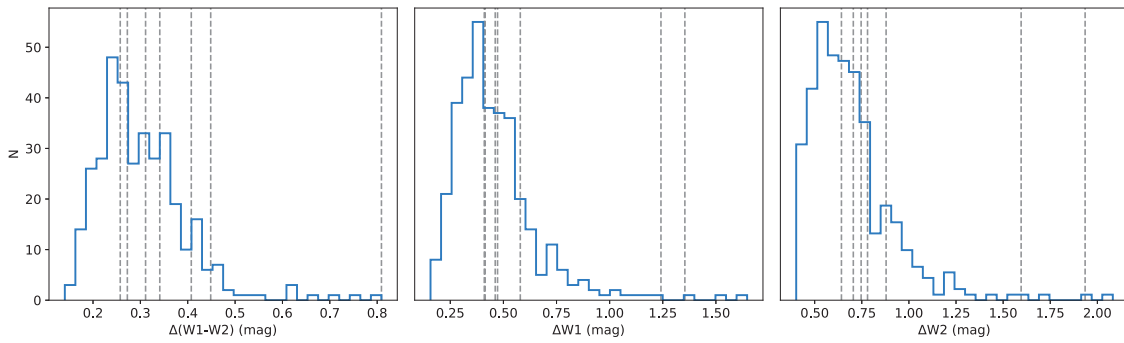


Figure 1. Distribution of the MIR variability of the sample. The left panel presents the maximum of MIR color variability, while the middle and right panel presents that of the $W1$ and $W2$, respectively. In each panel, the gray dashed line mark the seven candidates’ variability.

small separation to South Atlantic Anomaly (“SAA” < 5) and flagged moon masking (“moon mask” = 1), then binned the data in each epoch (nearly half year) using median value. We take the standard error of the median as the uncertainty. In order to compare with the optical light curves, we collected the Catalina Real-Time Transient Survey (CRTS) V band data (Drake et al. 2009), and the Palomar Transient Factory (PTF; Law et al. 2009) R band data. Also we grouped them using the median value in echo epoch as we did with the MIR data. The light curves are presented in the upper left panel of Figure 2.

2.3. Optical Spectra

All the seven candidates have an archive SDSS optical spectrum. We acquired another spectrum of J1307+4506, J1428+1723, and J1627+5419, using the Double Spectrograph (DBSP) of the Hale 5 m telescope (P200) at the Palomar Observatory on UT 2018 June 7. We selected the dichroic D55, the 600 line/mm (3780 Å blaze) grating on the blue camera, and the 316 line/mm (7150 Å blaze) grating on the red camera. J1307+4506 was split into two 900 s, while the other two were observed with two separated 600 s. All the three sources were exposed through a 1” slit. For the other four candidates J1252+5918, J1317+1024, J1549+1121, and J1713+2736, the spectra were obtained using the Kast DBSP at 3 m Shane telescope of Lick Observatory on UT 2018 June 12 and 13. We configured the instrument with a D57 dichroic, 600 line/mm (4310 Å blaze) grating on the blue arm and 600 line/mm (7500 Å blaze) grating on the red arm. The exposure of these four sources were split into three 600 s. J1317+1024 is observed through a 1”5 slit, while the others were through a 1” slit. All the data were reduced following the standard IRAF routine. The P200 spectra and J1317+1024 were calibrated using the standard star Feige56 obtained on the same night, while the other Shane spectra were calibrated by BD+28d4211. For the P200 spectra (J1307+4506, J1428+1723, and J1627+5419), the spectral resolution is $R \sim 1800\text{--}2190$. For the Shane spectra, the resolution of 1” slit (J1252+5918, J1549+1121, and J1713+2736) is $R \sim 2320\text{--}2690$, while the 1”5 slit (J1317+1024) is $R \sim 1890\text{--}2120$. So the resolution of DBSP is comparable with that of SDSS ($R \sim 1850\text{--}2200$, Shen et al. 2011). We plot the reduced spectra in the middle of Figure 2, and zoom in the $H\beta$ or $H\alpha$ region in the right panel. The P200 or Shane DBSP spectrum are scaled to the early SDSS epoch assuming the constant [O III] emission lines.

3. Method and Result

3.1. Spectral Decomposition

We use the Python QSO fitting code (PyQSOFit; Guo et al. 2018; Shen et al. 2019) to perform decomposition. With the help of PyQSOFit, the spectra are de-reddened, transformed to the rest frame, and decomposed into a host galaxy and quasar component with the principal component analysis method (Yip et al. 2004a, 2004b). Then we fit the quasar continuum with a power-law and polynomial model. The Fe II model is not used because there are no obvious Fe II emission lines in our sample. In order to get the best-fitting results of emission lines, we apply similar strategies as Liu et al. (2019) did, and we also use the P -value of F-distribution to test¹⁰ whether the fit is significantly improved by adding more components. For the Balmer emission lines, we use one single Gaussian to model the narrow component ($\text{FWHM} < 1200 \text{ km s}^{-1}$) and multiple (1 ~ 3) Gaussians to model the broad component ($\text{FWHM} > 1200 \text{ km s}^{-1}$). The multi-Gaussian scheme is adopted only if it can significantly improve the fit by $P_{F\text{-test}} < 0.05$. The number of broad components used is listed in column 9 of Table 1. When fitting the DBSP spectrum, the broad Balmer emission lines are assumed to have the same profile and redshift as those of SDSS or set to be free if it can significantly improve the fit by $P_{F\text{-test}} < 0.05$. For each spectrum, we generate 100 mock spectra by adding Gaussian noise to the original spectrum using the uncertainty of input data and repeat the fitting procedure. Finally, the standard deviation of the distributions of best-fitting is taken as the uncertainty for each spectral quantity. If there is no broad component for Balmer emission lines, we take the flux at 90% confidence level as the upper limit which is derived from $\Delta\chi^2 = 2.7$ (Avni 1976). The spectral properties are listed in column 10 ~ 13 of Table 1, and we present an example of decomposition in Figure 3.

3.2. Spectral Type Classification

As we know, Type 1 AGNs show both broad and narrow components of emission lines, while the Type 2 ones show only narrow components. The intermediate types have been introduced by Osterbrock (1977, 1981), which are based on the strength of the $H\beta$ and $H\alpha$ lines. In Type 1.5, the broad components are

¹⁰ The null hypothesis is that model 2 does not provide a significantly better fit than model 1. The P -value is used to prove against a null hypothesis. The smaller the P -value, the stronger the evidence that the null hypothesis should be rejected. If the P is lower than the critical value 0.05 of F-distribution, we reject the null hypothesis, which corresponds to a typical false rejection probability of 5%.

Table 1
Information of Seven AGNs

(1) Name	(2) Redshift	(3) Max $\Delta W1$ (mag)	(4) Max $\Delta W2$ (mag)	(5) $\log L_{5100,1}$ (erg s $^{-1}$)	(6) $\log L_{5100,2}$ (erg s $^{-1}$)	(7) S/N $_1$ (\AA^{-1})	(8) S/N $_2$ (\AA^{-1})	(9) Component	(10) $L_{H\beta,1}$ (10^{41} erg s $^{-1}$)	(11) $L_{H\beta,2}$ (10^{41} erg s $^{-1}$)	(12) $L_{H\alpha,1}$ (10^{41} erg s $^{-1}$)	(13) $L_{H\alpha,2}$ (10^{41} erg s $^{-1}$)	(14) S/N $_{H\beta_1}$	(15) S/N $_{H\beta_2}$	(16) S/N $_{H\alpha_1}$	(17) S/N $_{H\alpha_2}$	(18) T1	(19) T2
J125258.72 +591832.7	0.124	0.58 \pm 0.01	0.75 \pm 0.02	43.84 \pm 0.02	43.07 \pm 0.02	26.7	10.4	[2,2;1,2]	10.52 \pm 0.18	1.02 \pm 0.35	23.99 \pm 0.18	4.03 \pm 0.14	58.4	2.9	133.3	28.8	1	1.8
J130716.99 +450645.3	0.084	1.35 \pm 0.01	1.93 \pm 0.06	42.52 \pm 0.01	42.22 \pm 0.01	12.7	8.8	[1,2;0,0]	0.16 \pm 0.02	0.04*	0.61 \pm 0.04	0.07*	8.0	<1	15.3	<1	1	2
J142846.71 +172353.1	0.104	1.24 \pm 0.02	1.60 \pm 0.05	42.92 \pm 0.01	41.09 \pm 0.18	20.7	15.4	[1,1;0,0]	0.44 \pm 0.07	0.40*	3.61 \pm 0.06	0.65*	5.8	<1	51.5	<1	1	2
J131737.93 +102427.7	0.280	0.46 \pm 0.01	0.78 \pm 0.03	43.99 \pm 0.01	43.32 \pm 0.02	24.1	6.1	[1,2;0,...]	8.78 \pm 0.46	1.46*	33.26 \pm 0.79	...	19.1	<1	42.1	...	1	1.9
J162752.18 +541912.5	0.316	0.41 \pm 0.01	0.64 \pm 0.01	44.04 \pm 0.01	43.89 \pm 0.01	21.5	4.5	[1,3;0,1]	10.46 \pm 0.39	0.42*	78.90 \pm 2.90	62.04 \pm 6.19	14.1	<1	27.2	22.3	1	1.9
J171353.85 +273626.8	0.298	0.47 \pm 0.04	0.88 \pm 0.08	44.06 \pm 0.01	43.17 \pm 0.06	13.8	6.5	[2,1;1,...]	8.66 \pm 0.59	2.80 \pm 1.28	23.46 \pm 1.42	...	19.2	2.2	16.5	...	1	1.8
J154953.60 +112148.3	0.084	0.41 \pm 0.01	0.71 \pm 0.03	42.37 \pm 0.01	42.05 \pm 0.02	26.5	8.4	[0,1;0,1]	0.03*	0.02*	1.01 \pm 0.01	0.31 \pm 0.04	<1	<1	101.0	7.8	1.9	1.9

Note. The former three objects are CL AGNs, while the middle three objects are ambiguous. Column 3 presents the maximum of $\Delta W1$, while column 4 lists that of $\Delta W2$. $\log L_{5100,1}$, $L_{H\beta,1}$, and $L_{H\alpha,1}$ (in columns 5, 10, 12) represent the luminosity of 5100 \AA (in base-10 logarithm), $H\beta$, $H\alpha$ measured from the previous SDSS spectrum, while the $\log L_{5100,2}$, $L_{H\beta,2}$, and $L_{H\alpha,2}$ (in columns 6, 11, 13) measured from the recent DBSP spectrum. In columns 7 and 8, S/N $_1$ and S/N $_2$ are the median signal to noise at the 5500 \AA for the SDSS and DBSP spectrum. Column 9 lists the number of Gaussians adopted to fit the broad $H\beta$ and $H\alpha$. For example, $[n_1, n_2; n_3, n_4]$, the former two numbers mean that there are n_1 Gaussians used to fit the broad $H\beta$ and n_2 Gaussians used for broad $H\alpha$ in SDSS spectrum; and the latter two numbers n_3, n_4 are the number of Gaussians for broad $H\beta$ and $H\alpha$ in DBSP spectrum, respectively. In columns 14–17, S/N $_{H\beta_1}$ (S/N $_{H\alpha_1}$) and S/N $_{H\beta_2}$ (S/N $_{H\alpha_2}$) are the S/N of the broad $H\beta$ ($H\alpha$) component in the SDSS and DBSP, respectively. In columns 18 and 19, T1 and T2 respectively represent the spectral types of the SDSS and DBSP spectrum. For J1317+1024 and J1713+2736, their Shane DBSP spectra did not cover the $H\alpha$, so their $L_{H\alpha,2}$ is marked with a no data symbol “...”. The data note with “*” is the upper limit value at 90% confidence level which derived from $\Delta\chi^2 = 2.7$ (Avni 1976).

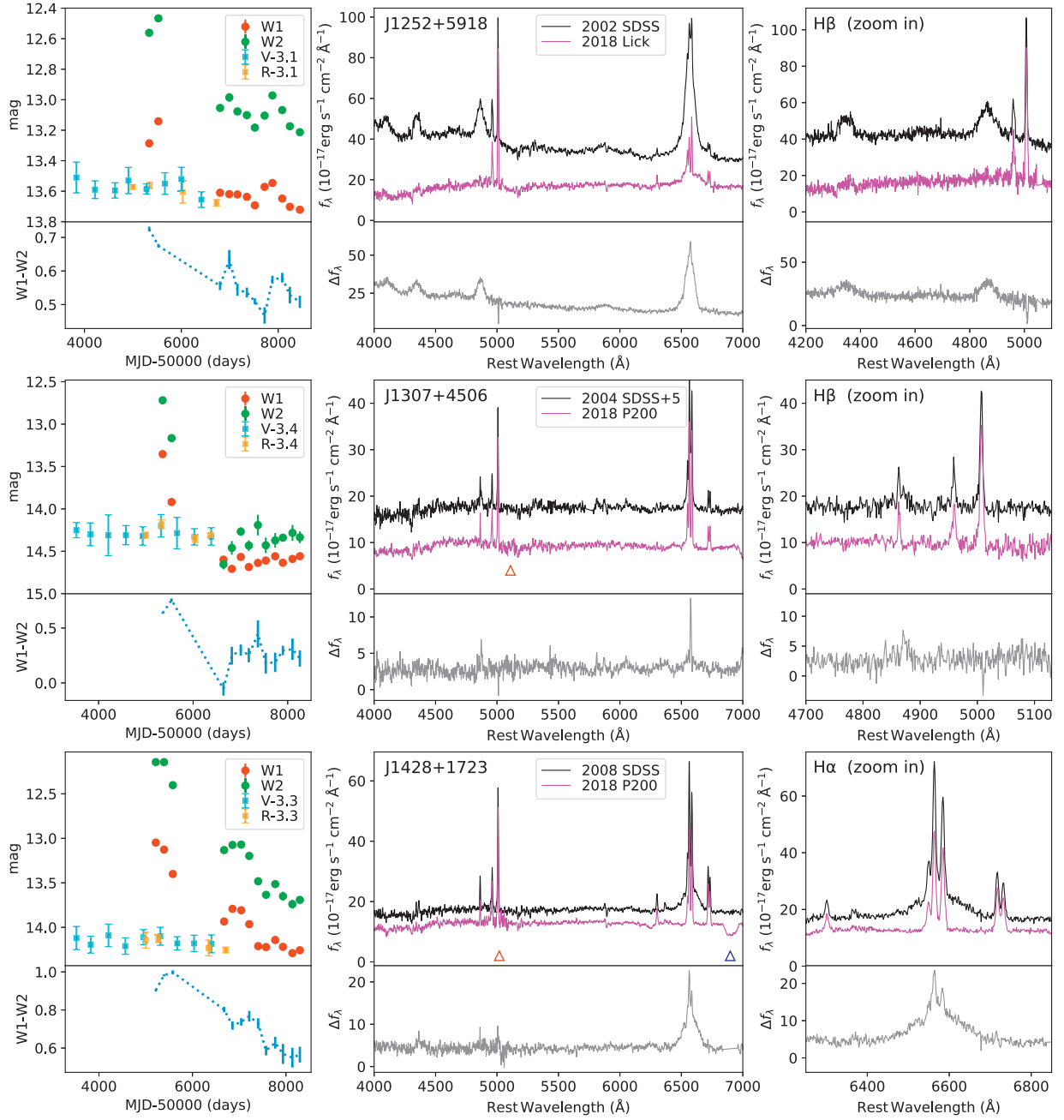


Figure 2. Light curves and spectra. In each figure, the upper left panel presents the mid-infrared and optical light curves. The red and green dots, respectively, represent the median value of $W1$ and $W2$ bands, while the blue and orange square represent the median of optical CRTS and PTF photometric data. The lower left panel presents the color of $W1-W2$. In the middle panel, the previous SDSS spectrum is plotted in black, while the recent DBSP spectrum is in magenta. The lower middle panel shows the difference of two spectra. The red triangle marks the position of the dichroic while the blue one marks uncorrected telluric. In the right panel, we zoom in the $H\beta$ or $H\alpha$ emission line. In addition, the spectra in the middle panel are smoothed by a flat window with a length of four pixels for good looking, but they are not smoothed in the right panel.

comparable at $H\beta$ and $H\alpha$ but the broad component of higher-order Balmer lines are very weak. In Type 1.8, the broad $H\beta$ is weak but no higher-order Balmer lines have a broad component, while Type 1.9 shows only a broad component in $H\alpha$ and not in higher-order Balmer lines. So we can simply use the signal-to-noise ratio (S/N) of broad $H\beta$ and $H\alpha$ lines to mark the AGN spectral types (Yang et al. 2018). If broad $H\beta$ is detected at an $S/N > 5\sigma$ level, we marked it as Type 1; if $H\alpha$ is detected at an $S/N > 5\sigma$ level, but $H\beta$ is at $S/N < 1\sigma$ ($1 \sim 3\sigma$, $3 \sim 5\sigma$), we marked it as Type 1.9 (1.8, 1.5); if there is no broad $H\alpha$ ($S/N < 1\sigma$), we marked it as Type 2.

With the spectrum decomposition, we find that J1317+1024, and J1627+5419 have turned from Type 1 into Type 1.9 due to their disappearance of broad $H\beta$ emission lines, while J1307+4506 and J1428+1723 even turned from Type 1 into Type 2 because no broad $H\alpha$ component presented in their DBSP spectrum. For J1252+5918 and J1713+2736, they turned into Type 1.8 because they still have a weak broad $H\beta$ component. For J1549+1121, it keeps Type 1.9 due to significant ($S/N_{H\alpha_2} = 7.8\sigma$) detectable broad $H\alpha$ in its Lick spectrum. We listed the detailed type transition in column 18 and 19 of Table 1.

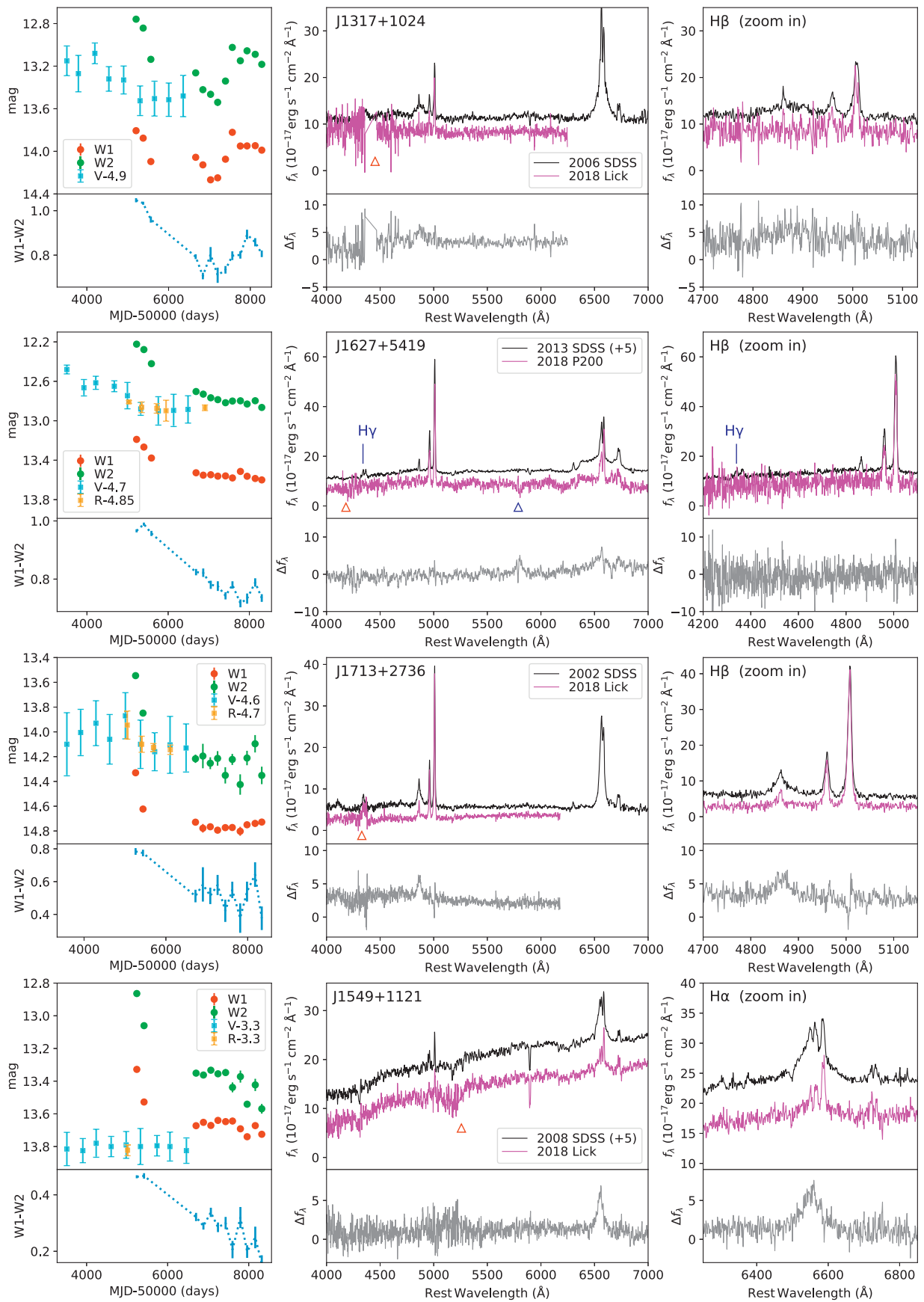


Figure 2. (Continued.)

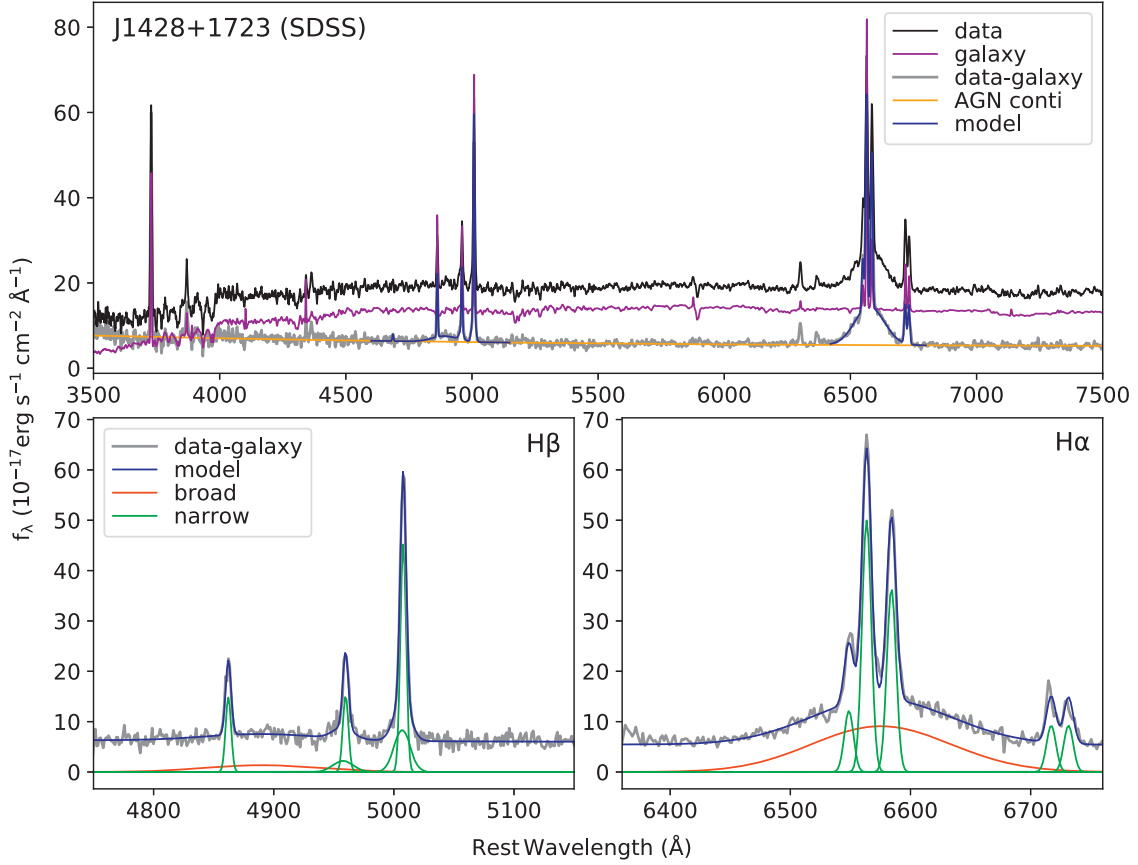


Figure 3. An example of spectral decomposition. In the top panel, the original SDSS spectrum of J1428+1723 is plotted in black. The host galaxy, AGN component, and continuum are in purple, gray, and orange, respectively. The model for AGN component is in blue. In the bottom panel, we show detailed components of the H β and H α . The broad components are in red while the narrow ones are in green.

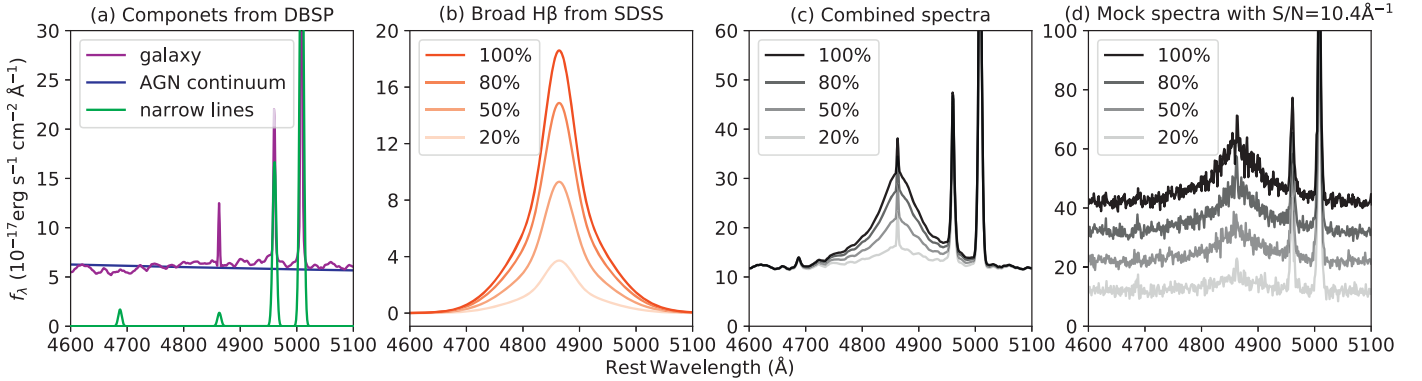


Figure 4. Process of mock J1252+5918's spectra with $S/N = 10.4 \text{ \AA}^{-1}$, and only the H β emission line region is presented as an example. (a) The galaxy, AGN continuum, and narrow emission line components extracted from J1252+5918's Lick spectrum. These components are combined as a mock spectrum with no broad H β emission line. (b) The broad H β component extracted from J1252+5918's SDSS spectrum. The red curves from high to low represent the 100%, 80%, 50%, and 20% of the broad H β flux, respectively. (c) The mock spectra combined by components presented in (a) and (b). (d) The final mock spectra with different proportions of broad H β whose S/N are set to that of J1252+5918's Lick spectrum (10.4 \AA^{-1}) by adding the random noise.

3.3. Test the Influence of Low Spectral S/N

CL AGNs are often identified by visual inspection of the spectra to see whether there is sharp change of broad Balmer emission lines. Apart from J1549+1121, the other six sources may be CL AGNs, for their H β luminosity shows significant decrease. However, it is not so robust to confirm the disappearance of the broad H β when it becomes very weak or the S/N of the spectrum is very low, especially for J1252+5918, J1317+1024, J1627+5419, and J1713+2736 whose

S/N at 5500 \AA decreases by more than 2 factors than that of the SDSS spectrum (see column 7, 8 in Table 1). So we perform a simulation to investigate the influence of low spectral S/N for the four objects. Figure 4 presents the simulation process of J1252+5918 as an example.

First, we construct a mock spectrum with no broad Balmer emission lines by combining the host galaxy, continuum, and narrow emission lines components from the decomposed DBSP spectrum (see Figure 4(a)). Second, we add the flux of

the broad Balmer components whose profiles are extracted from the corresponding SDSS spectrum. Then we construct four types of different spectra for each object by scaling the input flux of the SDSS broad $H\beta$ ($F_{H\beta,SDSS}$) at 100%, 80%, 50%, and 20% (Figures 4(b), (c)). By adding random noise, the S/N of the newly constructed spectrum is set to that of the original DBSP spectrum (Figure 4(d)). Finally, we use the PyQSOFit to decompose the constructed spectrum and fit the emission lines to test whether we can recover the input $F_{H\beta}$ (broad $H\beta$ component is adopted only when it can improve the fit by $P_{F-test} < 0.05$). We repeat the above procedure (both the spectrum construction and fitting) 500 times. We take the median value of recovered flux as the result and take the standard deviation as the uncertainty. In addition, the proportion of fit that can recover the broad $H\beta$ is taken as the significance. We briefly summarize the simulation results below.

- (1) J1252+5918: we can recover the “20% $\times F_{H\beta,SDSS}$ ” case at 100% level, and yield $L_{H\beta,recover} = 1.79 \pm 0.14$ ($10^{41} \text{erg s}^{-1}$), which is larger than the original $L_{H\beta,DBSP} = 1.02 \pm 0.35$ ($10^{41} \text{erg s}^{-1}$). So the relative low S/N of the J1252+5918’s DBSP spectrum has no influence on its flux detection, and it is a robust CL AGN.
- (2) J1317+1024: we can recover the “100% $\times F_{H\beta,SDSS}$ ” case at 99.2% level, which yields $L_{H\beta,recover} = 8.43 \pm 0.86$ ($10^{41} \text{erg s}^{-1}$), and recover the 80% $\times F_{H\beta,SDSS}$ case at 78.4%, which yields $L_{H\beta,recover} = 6.94 \pm 0.70$ ($10^{41} \text{erg s}^{-1}$). However, we can only recover the “50% $\times F_{H\beta,SDSS}$ ” case at 7% level.
- (3) J1627+5419: we failed to recover all the four cases.
- (4) J1713+2736: we can recover the “80% $\times F_{H\beta,SDSS}$ ” case at 98.2% level, which yields $L_{H\beta,recover} = 5.88 \pm 0.73$ ($10^{41} \text{erg s}^{-1}$), and the “50% $\times F_{H\beta,SDSS}$ ” case at 42.0% level, which yields $L_{H\beta,recover} = 3.82 \pm 0.44$ ($10^{41} \text{erg s}^{-1}$). However, we failed to recover the “20% $\times F_{H\beta,SDSS}$ ” case.

For J1317+1024, J1627+5419, and J1713+2736, the simulations show that the low S/N of their DBSP spectrum does impact on the flux detection, which means their late spectral type is ambiguous. So robustly, there are only three CL AGNs: J1252+5918, J1307+4506, and J1428+1723.

4. Discussion

According to the time interval between the SDSS and DBSP spectra, three objects, J1252+5918, J1307+4506, and J1428+1723, robustly transitioned from Type 1 to Type 1.8/2 during the timescale of $10 \sim 16$ yr. However, considering their decreasing tendency of the MIR light curves and color change, the CL transition timescale is likely $4 \sim 6$ yr in the observational frame, because they kept AGN-like color at MJD ~ 55500 , and turned galaxy-like around MJD ~ 57500 . While the mechanism of CL phenomenon is not fully understood, in our previous work (Sheng et al. 2017), we found both the large MIR variability amplitude (>0.4 mag) and the variation timescale (<5 yr) of 10 CL AGNs were against the scenario of varying obscuration. We preferred the scheme of dramatic change in the accretion rate (Sheng et al. 2017), which is also favored by the most CL studies (e.g., LaMassa et al. 2015; MacLeod et al. 2016; Ruan et al. 2016; Runnoe et al. 2016; Gezari et al. 2017; Stern et al. 2018; Yang et al. 2018; Guo et al. 2019, 2020). J1252+5918, J1307+4506, and J1428+1723 nearly have the same MIR behavior as

the turn-off CL AGNs in our previous work, and we assume that their type transition are also caused by dramatic accretion rate decrease. For the other four objects, they might also have significant accretion rate variation and change from high state into low state, but not low enough, because they also show significant MIR variability and color change in a short timescale but not a total disappearance of broad $H\beta$ or $H\alpha$ emission line.

All the seven sources have very similar variation behavior in MIR bands, because due to our selection criteria constraints the MIR light curves of candidates should feature a large decrease (>0.4 mag) tendency, along with the MIR color changing from AGN-like to galaxy-like. As we can see in the left panel of each subplot in Figure 2, the MIR light curves present the most significant variation before 57,000. However, the optical light curves show fewer variables than the MIR ones. Among seven AGNs, J1317+1024 and J1627+5419 have the most significant optical variation amplitude as 0.45 ± 0.17 and 0.42 ± 0.15 mag, while the others have a amplitude less than 0.2 mag, especially for the three AGNs that have robust spectral type transition. We checked their SDSS image and found that they are all extend sources. Their optical variability is likely highly diluted by the host galaxy. Considering the typical amplitude of the AGNs’ optical variability is ~ 0.2 mag, it is not easy to find them through the optical variability selection method (e.g., MacLeod et al. 2019 select CL AGNs candidates using $\Delta g > 1$ and $\Delta r > 0.5$ mag). The MIR variability is the hot-dust echo of the central continuum. So the CL AGNs’ MIR and optical variability are caused by the same physical mechanism (dramatic change of the accretion rate), which means there should not be a bias between the MIR and optical selecting method. However, for an extended source, the central continuum is easily diluted by the host galaxy. Compared with the optical CL AGNs selecting method, the MIR selecting method is likely to find more CL AGNs that are dominated by the host galaxy.

Our selection method benefits from the fact that MIR emission is much less affected by dust extinction than optical radiation. More importantly, the MIR emission of an AGN is dominated by the dust torus, which provides AGNs with characteristic red MIR colors and allows a simple $W1-W2$ color cut to robustly differentiate AGNs from stars and inactive galaxies (Richards et al. 2006; Stern et al. 2012; Assef et al. 2013). Our method could be a very efficient method to select CL AGNs based on MIR variability accompanied by the MIR color changing from AGN-like to galaxy-like. Previously, we found that CL AGNs show large MIR variability amplitude (>0.4 mag; Sheng et al. 2017). So one of our selecting criteria constrains that $W1$ or $W2$ should have a variability larger than 0.4 mag. If we set the criterion more strictly that both $W1$ and $W2$ should have >0.4 mag variation, there are 54% (191/353) fraction remaining, and these are CL AGNs at very high confidence. However, there might be some AGNs like J1549+1121 that maintain the spectral type. Although these objects are not often identified as CL AGNs, it is still interesting to investigate the mechanism of how they show such significant MIR variation (which is likely associated with the accretion rate) in short timescale ($5 \sim 6$ yr). There also might be some CL AGNs that turn-off first and re-brighten later on, but we identified them as maintaining spectral types due to the time delay between the MIR signal and the optical spectral transition. Considering the confirmation rate ($\geq 3/7$), there

might be more than 81 ($191 \times 3/7$) CL AGNs in our sample as soon as the full spectroscopic follow-up is carried out.

5. Summary

We present initial results from a systematic search for CL AGNs based on combining the MIR variation and color change. We started from an archival quasar spectrum catalog of SDSS and selected a large sample of candidates of CL AGNs. These sources have significant MIR variation (>0.4 mag) and change from AGN-like color into galaxy-like color at the same time. We followed seven candidates from our sample that are bright and proper for observation. Three objects (J1252+5918, J1307+4506, and J1428+1723) are robustly confirmed as turn-off CL AGNs, while three objects (J1317+1024, J1627+541, and J1713+2736) are not so robust to confirm suffering from low spectral quality. This work suggested that our selection method is likely to be an effective one to find CL AGNs. A large sample size of CL AGNs can provide us with an opportunity to statistically investigate the properties of CL AGNs. We will perform a statistical analysis of our sample (Z. F. Sheng et al. 2020, in preparation) and try to identify more CL AGNs. Moreover, our method can also be applied to select bulks of turn-on CL AGNs from galaxy catalogs, just alternatively constraining the $W1-W2$ changing from galaxy-like to AGN-like.

We acknowledge the anonymous referee for valuable comments that helped to improve the paper. This research uses data obtained through the Telescope Access Program (TAP), which has been funded by the National Astronomical Observatories, Chinese Academy of Sciences, and the Special Fund for Astronomy from the Ministry of Finance. Observations obtained with the Hale Telescope at Palomar Observatory were obtained as part of an agreement between the National Astronomical Observatories, Chinese Academy of Sciences, and the California Institute of Technology. This project is supported by National Natural Science Foundation of China (NSFC-11421303, NSFC-11603021, and NSFC-11833007). This research has made use of the NASA/ IPAC Infrared Science Archive, which is operated by the Jet Propulsion Laboratory, California Institute of Technology, under contract with the National Aeronautics and Space Administration. This publication makes use of data products from the Wide-field Infrared Survey Explorer, which is a joint project of the University of California, Los Angeles, and the Jet Propulsion Laboratory/California Institute of Technology, funded by the National Aeronautics and Space Administration. This publication also makes use of data products from *NEOWISE*, which is a project of the Jet Propulsion Laboratory/California Institute of Technology, funded by the Planetary Science Division of the National Aeronautics and Space Administration. This research made use of Astropy, a community-developed core Python package for Astronomy (Astropy Collaboration, Astropy Collaboration et al. 2013).

ORCID iDs

Zhenfeng Sheng  <https://orcid.org/0000-0001-6938-8670>
 Tinggui Wang  <https://orcid.org/0000-0002-1517-6792>
 Ning Jiang  <https://orcid.org/0000-0002-7152-3621>
 Jiani Ding  <https://orcid.org/0000-0003-4651-8510>
 Zheng Cai  <https://orcid.org/0000-0001-8467-6478>

Hengxiao Guo  <https://orcid.org/0000-0001-8416-7059>
 Liming Dou  <https://orcid.org/0000-0002-4757-8622>

References

- Assef, R. J., Prieto, J. L., Stern, D., et al. 2018a, *ApJ*, 866, 26
 Assef, R. J., Stern, D., Kochanek, C. S., et al. 2013, *ApJ*, 772, 26
 Assef, R. J., Stern, D., Noiro, G., et al. 2018b, *ApJS*, 234, 23
 Astropy Collaboration, Robitaille, T. P., Tollerud, E. J., et al. 2013, *A&A*, 558, A33
 Avni, Y. 1976, *ApJ*, 210, 642
 Bon, E., Zucker, S., Netzer, H., et al. 2016, *ApJS*, 225, 29
 Cohen, R. D., Puetter, R. C., Rudy, R. J., Ake, T. B., & Foltz, C. B. 1986, *ApJ*, 311, 135
 Denney, K. D., De Rosa, G., Croxall, K., et al. 2014, *ApJ*, 796, 134
 Dexter, J., & Begelman, M. C. 2019, *MNRAS*, 483, L17
 Drake, A. J., Djorgovski, S. G., Mahabal, A., et al. 2009, *ApJ*, 696, 870
 Eracleous, M., & Halpern, J. P. 2001, *ApJ*, 554, 240
 Gezari, S., Chornock, R., Rest, A., et al. 2012, *Natur*, 485, 217
 Gezari, S., Hung, T., Cenko, S. B., et al. 2017, *ApJ*, 835, 144
 Goodrich, R. W. 1989, *ApJ*, 340, 190
 Guo, H., Shen, Y., He, Z., et al. 2020, *ApJ*, 888, 58
 Guo, H., Shen, Y., & Wang, S. 2018, PyQSOFit: Python code to fit the spectrum of quasars, Astrophysics Source Code Library, ascl:1809.008
 Guo, H., Sun, M., Liu, X., et al. 2019, *ApJL*, 883, L44
 Hutmekers, D., Agís González, B., Marin, F., et al. 2019, *A&A*, 625, A54
 Hutmekers, D., Agís González, B., Sluse, D., Ramos Almeida, C., & Acosta Pulido, J.-A. 2017, *A&A*, 604, L3
 Jiang, N., Dou, L., Wang, T., et al. 2016, *ApJL*, 828, L14
 Jiang, N., Zhou, H.-Y., Ho, L. C., et al. 2012, *ApJL*, 759, L31
 Jun, H. D., Stern, D., Graham, M. J., et al. 2015, *ApJL*, 814, L12
 LaMassa, S. M., Cales, S., Moran, E. C., et al. 2015, *ApJ*, 800, 144
 Law, N. M., Kulkarni, S. R., Dekany, R. G., et al. 2009, *PASP*, 121, 1395
 Lawrence, A. 2018, *NatAs*, 2, 102
 Liu, H.-Y., Liu, W.-J., Dong, X.-B., et al. 2019, *ApJS*, 243, 21
 MacLeod, C. L., Green, P. J., Anderson, S. F., et al. 2019, *ApJ*, 874, 8
 MacLeod, C. L., Ross, N. P., Lawrence, A., et al. 2016, *MNRAS*, 457, 389
 Mainzer, A., Bauer, J., Cutri, R. M., et al. 2014, *ApJ*, 792, 30
 Martini, P., & Schneider, D. P. 2003, *ApJL*, 597, L109
 Merloni, A., Dwelly, T., Salvato, M., et al. 2015, *MNRAS*, 452, 69
 Oknyansky, V. L., Winkler, H., Tsygankov, S. S., et al. 2019, *MNRAS*, 483, 558
 Osterbrock, D. E. 1977, *ApJ*, 215, 733
 Osterbrock, D. E. 1981, *ApJ*, 249, 462
 Pâris, I., Petitjean, P., Aubourg, É., et al. 2018, *A&A*, 613, A51
 Pâris, I., Petitjean, P., Ross, N. P., et al. 2017, *A&A*, 597, A79
 Rees, M. J. 1988, *Natur*, 333, 523
 Richards, G. T., Lacy, M., Storrie-Lombardi, L. J., et al. 2006, *ApJS*, 166, 470
 Ruan, J. J., Anderson, S. F., Cales, S. L., et al. 2016, *ApJ*, 826, 188
 Ruan, J. J., Anderson, S. F., Eracleous, M., et al. 2019, *ApJ*, 883, 76
 Rumbaugh, N., Shen, Y., Morganson, E., et al. 2018, *ApJ*, 854, 160
 Runco, J. N., Cosens, M., Bennert, V. N., et al. 2016, *ApJ*, 821, 33
 Runnoe, J. C., Cales, S., Ruan, J. J., et al. 2016, *MNRAS*, 455, 1691
 Schneider, D. P., Richards, G. T., Hall, P. B., et al. 2010, *AJ*, 139, 2360
 Sergeev, S. G., Doroshenko, V. T., Dzyuba, S. A., et al. 2007, *ApJ*, 668, 708
 Shappee, B. J., Prieto, J. L., Grupe, D., et al. 2014, *ApJ*, 788, 48
 Shen, Y., Hall, P. B., Horne, K., et al. 2019, *ApJS*, 241, 34
 Shen, Y., Richards, G. T., Strauss, M. A., et al. 2011, *ApJS*, 194, 45
 Sheng, Z., Wang, T., Jiang, N., et al. 2017, *ApJL*, 846, L7
 Śniegowska, M., & Czerny, B. 2019, arXiv:1904.06767
 Stern, D., Assef, R. J., Benford, D. J., et al. 2012, *ApJ*, 753, 30
 Stern, D., McKernan, B., Graham, M. J., et al. 2018, *ApJ*, 864, 27
 Storchi-Bergmann, T., Baldwin, J. A., & Wilson, A. S. 1993, *ApJL*, 410, L11
 Taylor, M. B. 2005, in ASP Conf. Ser. 347, *Astronomical Data Analysis Software and Systems XIV*, ed. P. Shopbell, M. Britton, & R. Ebert (San Francisco, CA: ASP), 29
 Tran, H. D., Osterbrock, D. E., & Martel, A. 1992, *AJ*, 104, 2072
 Wang, J., Xu, D. W., & Wei, J. Y. 2018, *ApJ*, 858, 49
 Wright, E. L., Eisenhardt, P. R. M., Mainzer, A. K., et al. 2010, *AJ*, 140, 1868
 Yan, L., Donoso, E., Tsai, C.-W., et al. 2013, *AJ*, 145, 55
 Yang, Q., Wu, X.-B., Fan, X., et al. 2018, *ApJ*, 862, 109
 Yip, C. W., Connolly, A. J., Szalay, A. S., et al. 2004a, *AJ*, 128, 585
 Yip, C. W., Connolly, A. J., Vanden Berk, D. E., et al. 2004b, *AJ*, 128, 2603